

## Article

# Correlation between Turbidity and Inherent Optical Properties as an Initial Recognition for Backscattering Coefficient Estimation

Kamila Haule <sup>1,\*</sup> , Maria Kubacka <sup>2</sup> , Henryk Toczek <sup>1</sup> , Barbara Lednicka <sup>1</sup> , Bogusław Pranszke <sup>1</sup> and Włodzimierz Freda <sup>1</sup> 

<sup>1</sup> Department of Physics, Gdynia Maritime University, ul. Morska 81-87, 81-225 Gdynia, Poland; h.toczek@wm.umg.edu.pl (H.T.); b.lednicka@wm.umg.edu.pl (B.L.); b.pranszke@wm.umg.edu.pl (B.P.); w.freda@wm.umg.edu.pl (W.F.)

<sup>2</sup> Department of Operational Oceanography, Maritime Institute, Gdynia Maritime University, ul. Długi Targ 41/42, 80-830 Gdańsk, Poland; mkubacka@im.umg.edu.pl

\* Correspondence: k.haule@wm.umg.edu.pl

**Abstract:** Seawater turbidity is a common water quality indicator measured in situ and estimated from space on a regular basis. However, it is rarely correlated with the inherent optical properties of seawater, which convey information about seawater composition. In this study, we show a simple application of the turbidimeter's weighting function in the estimation of the backscattering coefficient of a model inorganic suspension in seawater. First, we introduce a method to measure the instrument's weighting function which describes the sensor's angular response in terms of scattering angles. The determination of the sensor-specific weighting function led us to characterize its angular sensitivity to the presence of suspended particles. The highest sensitivity for the Seapoint turbidimeter is in the range of 114°–128° (containing 25% of the total signal). Next, we describe the correlations between turbidity and the scattering and backscattering coefficients on the example of the model of inorganic particle suspension using the calculations based on Mie theory. The correlations are analyzed for narrow size fractions of the particle size distribution of silica in the range of 0.59–190 μm. We established that there is a good linear correlation (characterized by the coefficient of determination  $r^2 = 0.979$ ) between the part of the scattering coefficient measured by the turbidimeter and the backscattering coefficient of all size fractions of the model inorganic suspension.

**Keywords:** turbidity; turbidimeter; weighting function; suspended particles; inorganic suspension; light scattering; particle size distribution; water quality; seawater



**Citation:** Haule, K.; Kubacka, M.; Toczek, H.; Lednicka, B.; Pranszke, B.; Freda, W. Correlation between Turbidity and Inherent Optical Properties as an Initial Recognition for Backscattering Coefficient Estimation. *Water* **2024**, *16*, 594. <https://doi.org/10.3390/w16040594>

Academic Editor: Achim A. Beylich

Received: 17 January 2024

Revised: 9 February 2024

Accepted: 15 February 2024

Published: 17 February 2024



**Copyright:** © 2024 by the authors. Licensee MDPI, Basel, Switzerland. This article is an open access article distributed under the terms and conditions of the Creative Commons Attribution (CC BY) license (<https://creativecommons.org/licenses/by/4.0/>).

## 1. Introduction

According to the Water Framework Directive [1], the quality elements for the classification of ecological status include thermal, oxygenation, and nutrient conditions, as well as salinity, acidification status, and transparency. The oldest and still popular method of measuring water transparency is the determination of the Secchi depth (SD) by lowering the Secchi disk (white or black and white disk with a diameter of 20–30 cm) into the water until it is no longer visible to the observer [2,3]. The SD describes the spatial variability of water properties and is closely related to the absorption and scattering of underwater light [4]. It is widely accepted as a good indicator of eutrophication [5].

Nowadays, both transparency and turbidity are well-known indicators of water quality [6]. Widely available multiparameter underwater probes are equipped with modern sensors for measuring turbidity, which express the scattered light resulting from the interaction of incident light with particulate material in a liquid sample [7,8]. The scattering process changes the direction of light rays on randomly distributed optical inhomogeneities of the medium [9]. In the natural marine environment, such inhomogeneities are suspended in dissolved substances: clay, silt, pine pollen, finely divided organic matter, plankton, other microscopic organisms, floating debris, oil droplets, organic acids, pigments, and

air bubbles [7,10–15]. The increase in the amount of admixed components reduces water quality and transparency and, consequently, causes higher turbidity levels. The size of suspension particles or bubbles has a significant influence on optical measurements, including turbidity measurements [7,16–18].

A device that measures turbidity is called a turbidimeter. Currently, there is a large selection of turbidimeters on the market, which are generally categorized as absorptiometers and nephelometers [13,19]. The measurements can be performed in the laboratory on collected water samples, taken from the ship in the entire section of the water column, or can be constantly recorded by a sensor installed on a hydrographic platform or buoy. Turbidimeters have various designs and modes of operation—based on attenuation or scattering detection, different light sources, beam configurations, angular range, and the spectral sensitivity of detectors [17,19–21].

Raw data from differently designed instruments should not be considered directly interchangeable as the turbidity reporting units correspond with turbidity sensor design. This means that the turbidity, measured with instruments of different optical configurations, may differ for the same environmental sample [13,17,22,23]. A detailed compilation of turbidity reporting units (Table 1) was provided by Anderson [17].

**Table 1.** Reporting units corresponding to turbidity instrument designs (Table 6.7–4. in [17]).

Detector Geometry	Light Wavelength	
	White or Broadband (with a Peak Spectral Output of 400–680 nm)	Monochrome (Spectral Output Typically Near-Infrared, 780–900 nm)
Single Illumination Beam Light Source		
At 90° to the incident beam	Nephelometric Turbidity Unit (NTU) <sup>1</sup> (P63675)	Formazin Nephelometric Unit (FNU) <sup>2</sup> (P63680)
At 90° and other angles. An instrument algorithm uses a combination of detector readings, which may differ for values of varying magnitude	Nephelometric Turbidity Ratio Unit (NTRU) (P63676)	Formazin Nephelometric Ratio Unit (FNRU) (P63681)
At 30° ± 15° to the incident beam (backscatter)	Backscatter Unit (BU) (P63677)	Formazin Backscatter Unit (FBU) (P63682)
At 180° to the incident beam (attenuation)	Attenuation Unit (AU) (P63678)	Formazin Attenuation Unit (FAU) (P63683)
Multiple illumination beam light source		
At 90° and possibly other angles to each beam. An instrument algorithm uses a combination of detector readings, which may differ for values of varying magnitude	Nephelometric Turbidity Multibeam Unit (NTMU) (P63679)	Formazin Nephelometric Multibeam Unit (FNMU) (P63684)

<sup>1</sup> EPA Method 180.1 defines the optical geometry for NTU measurements. The detector angle must be 90° ± 30 to the incident light beam. The light source must be a tungsten lamp with a color temperature of 2200–3000 K [24].

<sup>2</sup> ISO 7027 defines the optical geometry for FNU measurements. The detector angle must be 90° ± 2.5 to the incident light beam. The light source must be a light-emitting diode (LED) with a wavelength of 860 ± 60 nm [25].

A comprehensive overview of turbidimeters, their operating principles, and stated accuracies was presented by Rymaszewicz [19], who tested twelve commercially available instruments to assess their traceability in comparison with previously prepared suspensions with known suspended solids concentrations. This experiment showed a large discrepancy in the responses of optical turbidimeters, regardless of the principle of their operation. It is considered that the 90° detection angle is the most sensitive angle to measure scattered light, characterized by the quasi-linear correlation between turbidity and light intensity for small turbidity values [16,22]. Thus, turbidity is most commonly expressed in a NTU

(Nephelometric Turbidity Unit) or FNU (Formazin Nephelometric Unit). In the existing literature related to the study of the natural environment, the results of turbidity measurements are most often expressed in these units [23,24]. However, in some papers, the authors measure and analyze turbidity in Formazin Turbidity Units (FTU) [12,25–27]. The FTU became a defined unit after the acceptance of Formazin as the primary reference standard for turbidity measurement, however, the FTU does not specify how a device measures turbidity in a water sample. Still, there is a lack of specificity in the influence of the ambient conditions and sensor configuration on the measurements in different instruments [28,29].

Turbidity measurements in natural ocean waters typically provide results in the range of below 1 NTU for oligotrophic waters to several NTU for eutrophic waters depending on chlorophyll concentration. These values for coastal waters can be as high as 10 NTU, while in estuaries they may exceed 100 NTU [29,30] or even 10,000 NTU in extremely turbid waters [31]. Typical turbidity values in natural open sea waters allow us to assume with a good approximation that in the range of optical path, which in most turbidimeters is 1–10 cm long, there will be no phenomenon of particle obscuration or multiple scattering. This is why we can assume that turbidity is a measurement of a fragment of the volume scattering function (VSF), around the scattering angle of 90°. Therefore, there is a question of whether the measurement made with a turbidimeter can be described by the inherent optical properties (IOPs) of ocean water.

To address this question, this study focused on the following research objectives:

- Determining the angular weighting function that would define what part of the volume scattering function is recorded by the turbidity meter. This function will be defined as  $\gamma(\theta)$  in the next chapter;
- Determining angular scattering properties, as well as the magnitude of the signal, measured by the turbidity meter for different fractions of the model suspension;
- Finding the correlation of the turbidimeter signal with elements of the scattering properties of the suspension.

## 2. Materials and Methods

### 2.1. Mathematical Description of Turbidity under Single Scattering Regime

In environmental optics, the light scattering coefficient of suspended particulate matter ( $b_p$ ) measured in  $\text{m}^{-1}$  is applied to describe the optical properties of the analyzed medium [9,32]. Due to the assumed homogeneity of scattering around the optical axis, the  $b_p$  is defined as the integral of the volume scattering function (VSF) over the full solid angle:

$$b_p = 2\pi \int_0^\pi \beta_p(\theta) \cdot \sin\theta d\theta, \quad (1)$$

where  $\beta_p(\theta)$  is the particle VSF of scatterers and  $\theta$  is the scattering angle. The backscattering coefficient ( $b_{bp}$ ) is defined as the integral of the VSF over the scattering angles of 90° to 180°:

$$b_{bp} = 2\pi \int_{\pi/2}^\pi \beta_p(\theta) \cdot \sin\theta d\theta. \quad (2)$$

The quotient of the particle backscattering coefficient and the scattering coefficient called the backscattering ratio ( $B_p$ ), describes the probability that, as a result of scattering, a photon will hit the backward hemisphere, and it is defined as:

$$B_p = \frac{b_{bp}}{b_p} \quad (3)$$

A turbidimeter measures the intensity of light scattered into some angles. Depending on the relative position of the sample illumination window and the detector window, as well as the shape of the measurement chamber, the angles at which the scattered light reaches the detector can be characterized using various weighting functions  $\gamma(\theta)$ . Using the inherent optical properties, the signal registered by the turbidimeter ( $b_{turb}$ ), may be described by the following part of the scattering coefficient  $b_p$ :

$$b_{turb} = 2\pi \int_0^\pi \beta_p(\theta) \cdot \gamma(\theta) \cdot \sin\theta d\theta \quad (4)$$

where  $\gamma(\theta)$  is a dimensionless weighting function of the turbidimeter, which depends on the scattering angle  $\theta$ . In fact, this dimensionless function describes the angular probability distribution of the turbidity measurement made under single scattering conditions. It is unique for every device and provides information on the contribution of recorded signals from different angles. In our experiment,  $\gamma(\theta)$  was determined during laboratory tests (Section 2.2). The determination of the turbidimeter's weighting function allows us to link turbidity measurement to the inherent optical properties of the water sample.

Under single scattering conditions, when the detector receives light from scattering on the first suspended particle encountered in a water sample, the turbidity signal ( $T$ ) will be proportional to the part of the scattering coefficient defined above as  $b_{turb}$ :

$$b_{turb} = const \cdot T \quad (5)$$

For turbidity  $T$  measured in FTU, the proportionality factor would be expressed in  $FTU^{-1} \cdot m^{-1}$ .

## 2.2. Measurements of the Angular Weighting Function

For the experiment, the SAIV SD204 CTD/STD probe (SAIV A/S, Bergen, Norway) was used, which was equipped with a turbidity meter manufactured by Seapoint Sensors Inc. (Exeter, NH, USA). It is a small-size turbidity sensor suitable for in-water measurements up to 6000 m depth characterized by a low-temperature coefficient of  $<0.05\%/^{\circ}C$  and a relatively low sensing distance of 5 cm from optical windows. The sensor can be operated in four selectable ranges: 12.5, 62.5, 250, and 750 FTU—characterized by supplier-declared signal linearity of  $<2\%$  deviation in the range of 0–1250 FTU. The instrument is equipped with an LED light source that emits a light wavelength of 880 nm (near-infrared range). Detectors are silicon photodiodes with visible-light-blocking filters. Thus, the detector can register light scattered by sample particles at angles of  $15^{\circ}$  to  $150^{\circ}$ .

The determination of the gamma function was based on measurements taken on a specially prepared test stand (Figure 1). In front of the probe, a 0.5 mm thick and 10 cm long steel rod was placed, which was mounted on a frame that could be shifted up and down, as well as moved towards and away from the optical windows. The probe recorded turbidity values generated by the steel rod ( $T_{rod}$ ). The sliders were equipped with fine threads enabling the reading of changes in the position of the rod with an accuracy of 0.02 mm. The turbidity sensor and the sliding bar were immersed in MilliQ water.

Measurements were taken in an area of  $24 \times 32$  mm covering the turbidimeter field of view. The majority of measurements were made within a range of 62.5 FTU, however, after bringing the rod to the windows at a distance of less than 8 mm, the recorded signal exceeded the originally selected range. Measurements in the square area of  $8 \times 8$  mm closest to the turbidimeter windows were made within a range of 250 FTU. Turbidity was recorded every 1 mm in a vertical direction and every 2 mm in a horizontal direction.

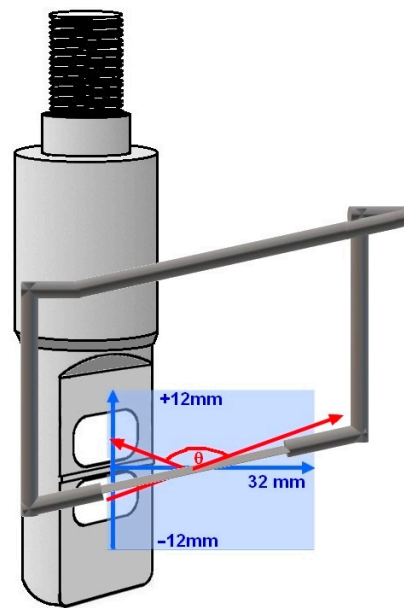


**Figure 1.** The design of the test stand for measuring the angular weighting function of the turbidimeter.

### 2.3. Model of Inorganic Particle Suspension

To demonstrate the application of the angular weighting function of the turbidimeter, a model particle suspension was developed and mathematical calculations of the inherent optical properties were performed based on the Mie solution [33]. This is the solution to Maxwell's equations (also known as the Lorenz-Mie solution) and describes the scattering of an electromagnetic wave on homogeneous spheres. The solution was suggested by Gustav Mie a long time ago, in 1908 [33], but it was not until the use of computer algorithms [34] that the calculations could be repeatedly duplicated for a wide range of scattering particle sizes. Thus, Mie scattering could be used as a scattering approximation for aerosols and aqueous suspensions.

According to the assumptions of the Mie solution, a homogeneous suspension of inorganic spherical particles was developed, which was characterized by a particle size distribution (*PSD*) similar to the natural distributions in the marine environment. The *PSD* of our model suspension is described by the power-law function according to [35]. This function was approximated using the single-segment power law:

$$PSD(d) = 1.17 \cdot 10^5 \cdot d^{-4.25}, \quad (6)$$

where  $d$  is the particle diameter and *PSD* is the number of particles in 1 cubic centimeter per 1  $\mu\text{m}$  range of particle diameters.

Next, we divided this particle size distribution into 22 narrow-size fractions starting from 0.59  $\mu\text{m}$  with a multiplier of 1.3. The first fraction had a diameter range of 0.59 to 0.77  $\mu\text{m}$ , and the last one of 146 to 190  $\mu\text{m}$ . Each fraction was, therefore, assigned a different concentration of particles (see Table 2). Then, for every size fraction, the  $b_p$  and the VSF were computed. Despite the assumption of ideal sphericity of particles, the application of the Mie solution provides precise results, particularly for particles with surface irregularities smaller than the wavelength of 880 nm. The optical properties of the model inorganic suspension are determined by its complex refractive index [35]. Clay minerals are the most typical inorganic substances found in natural water bodies. They are composed essentially of silica with the addition of aluminum, magnesium, or iron in varying degrees, and sometimes potassium, sodium, and calcium [36]. This is why we chose silica ( $\text{SiO}_2$ ) as the representative compound, which can be found in large amounts in the natural inorganic suspension.

**Table 2.** The concentration of particles, scattering, and backscattering coefficients for each of the 22 fractions of PSD.

Fraction Number	Diameter Range [ $\mu\text{m}$ ]	Concentration [ $\text{m}^{-3}$ ]	Scattering Coefficient $b_p$ [ $\text{m}^{-1}$ ]	Backscattering Coefficient $b_{bp}$ [ $\text{m}^{-1}$ ]
1	0.59–0.77	$1.13 \times 10^{11}$	$7.16 \times 10^{-3}$	$1.69 \times 10^{-4}$
2	0.77–1	$4.85 \times 10^{10}$	$9.18 \times 10^{-3}$	$1.16 \times 10^{-4}$
3	1–1.30	$2.07 \times 10^{10}$	$1.13 \times 10^{-2}$	$9.42 \times 10^{-5}$
4	1.30–1.69	$8.80 \times 10^9$	$1.37 \times 10^{-2}$	$7.28 \times 10^{-5}$
5	1.69–2.20	$3.75 \times 10^9$	$1.59 \times 10^{-2}$	$6.11 \times 10^{-5}$
6	2.20–2.86	$1.60 \times 10^9$	$1.74 \times 10^{-2}$	$5.10 \times 10^{-5}$
7	2.86–3.71	$6.82 \times 10^8$	$1.74 \times 10^{-2}$	$4.51 \times 10^{-5}$
8	3.71–4.83	$2.91 \times 10^8$	$1.45 \times 10^{-2}$	$4.06 \times 10^{-5}$
9	4.83–6.28	$1.24 \times 10^8$	$8.78 \times 10^{-3}$	$3.67 \times 10^{-5}$
10	6.28–8.16	$5.28 \times 10^7$	$3.85 \times 10^{-3}$	$3.38 \times 10^{-5}$
11	8.16–10.6	$2.25 \times 10^7$	$2.73 \times 10^{-3}$	$3.09 \times 10^{-5}$
12	10.6–13.8	$9.60 \times 10^6$	$2.43 \times 10^{-3}$	$2.90 \times 10^{-5}$
13	13.8–17.9	$4.09 \times 10^6$	$1.41 \times 10^{-3}$	$2.22 \times 10^{-5}$
14	17.9–23.3	$1.74 \times 10^6$	$1.03 \times 10^{-3}$	$1.32 \times 10^{-5}$
15	23.3–30.3	$7.43 \times 10^5$	$7.14 \times 10^{-4}$	$5.67 \times 10^{-6}$
16	30.3–39.4	$3.17 \times 10^5$	$4.94 \times 10^{-4}$	$2.85 \times 10^{-6}$
17	39.4–51.2	$1.35 \times 10^5$	$3.31 \times 10^{-4}$	$1.66 \times 10^{-6}$
18	51.2–66.5	$5.76 \times 10^4$	$2.33 \times 10^{-4}$	$7.77 \times 10^{-7}$
19	66.5–86.5	$2.45 \times 10^4$	$1.63 \times 10^{-4}$	$3.94 \times 10^{-7}$
20	86.5–112	$1.05 \times 10^4$	$1.20 \times 10^{-4}$	$2.06 \times 10^{-7}$
21	112–146	$4.46 \times 10^3$	$9.27 \times 10^{-5}$	$1.23 \times 10^{-7}$
22	146–190	$1.90 \times 10^3$	$7.24 \times 10^{-5}$	$8.12 \times 10^{-8}$

The Seapoint turbidimeter is powered by infrared light with a wavelength of 880 nm and at this wavelength, the refractive index of silica is  $n = 1.45998$ , and the imaginary part is  $k = 0.0011858i$  [37]. Both the particle size distribution and the complex refractive index were the input data for the Mie calculations.

### 3. Results

#### 3.1. The Turbidimeter's Angular Weighting Function

The turbidimeter's weighting function was measured to characterize the strength of the output signal received from different angles. While moving the steel rod in the vertical and horizontal planes, turbidity values  $T_{rod}$  in FTU were recorded. The resulting data set was interpolated using the kriging method in the Surfer by Golden software program to obtain the vertical cross-section of the turbidity distribution (Figure 2). The measured values varied from 0.39 FTU on the periphery of the area analyzed to as much as 97.38 FTU recorded at a distance of 6 mm from the probe at the central height between the emitter and the detector windows. The minimal value of 0.39 FTU was taken as the measurement background and subtracted from all results so that the measured values represented only the result of infrared light scattering from the rod.

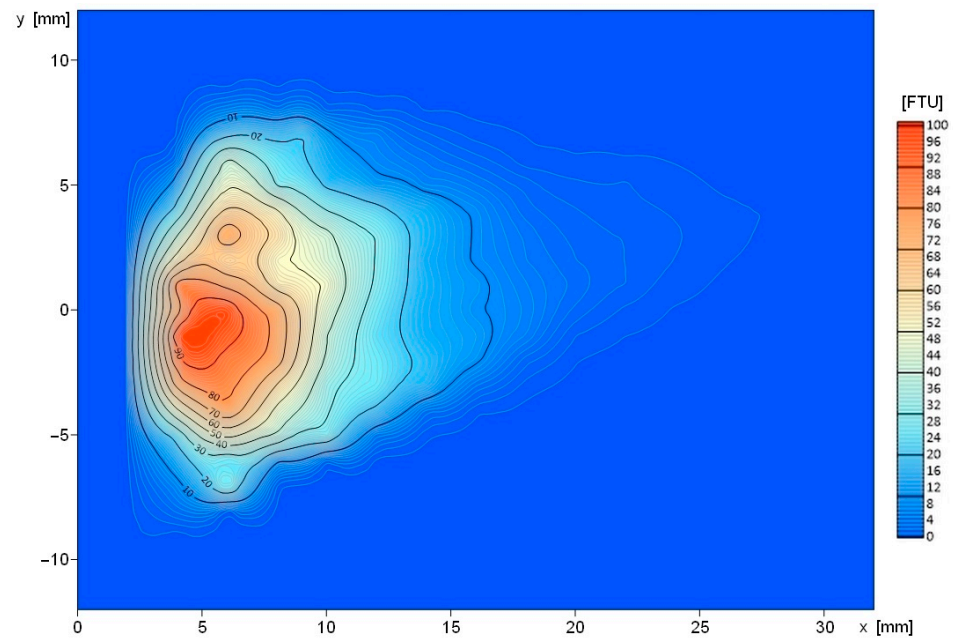


**Figure 2.** The spatial distribution of turbidity caused by light scattering from the rod placed in front of the turbidimeter in MilliQ water.

Converting the spatial turbidity distribution into an angular probability function required a linear interpolation between the points. After linear interpolation, made in MATLAB, results were obtained for a grid with a pixel size of 0.02 mm. For each of these pixels, the angle between the centers of the two turbidimeter windows was determined. Pixels were assigned the same scattering angle lie on arcs, passing through the centers of the illuminating and recording windows (see Figure 3). Interpolated turbidity values  $T_{rod}$  were integrated for each angle range of  $\theta - \Delta\theta$  to  $\theta + \Delta\theta$  and normalized to unity according to the formula:

$$\gamma(\theta) = \frac{\int_{\theta-\Delta\theta}^{\theta+\Delta\theta} T_{rod} d\theta}{\int_0^\pi T_{rod} d\theta}, \tag{7}$$

where interval  $\Delta\theta$  was set as  $0.5^\circ$ .

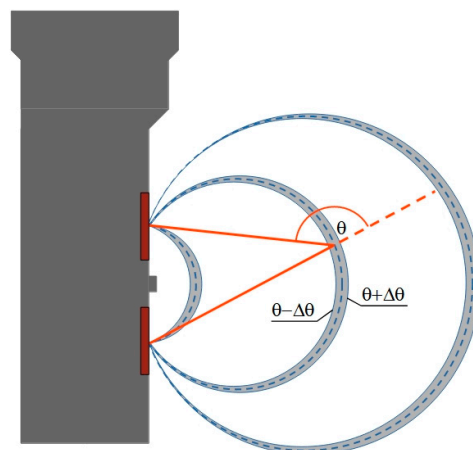


**Figure 3.** Visualization of contribution to the turbidimeter signal from different scattering angles  $\theta$ .

The obtained function is the turbidimeter’s weighting function, plotted in Figure 4. The weighting function  $\gamma(\theta)$  indicates the range of scattering angles measured by the sensor and depends only on the instrument and not on the suspended particles in the sample. It characterizes the angles which have the greatest contributions to the measured value.

For the Seapoint turbidimeter, it takes the values below  $10^{-4}$  for angles lower than  $18^\circ$  and above  $156^\circ$ . The highest value, which is 0.0159, is obtained for an angle of  $120^\circ$ . The resulting peak is also characterized by an extensive full width at half maximum (FWHM) of  $55^\circ$ .

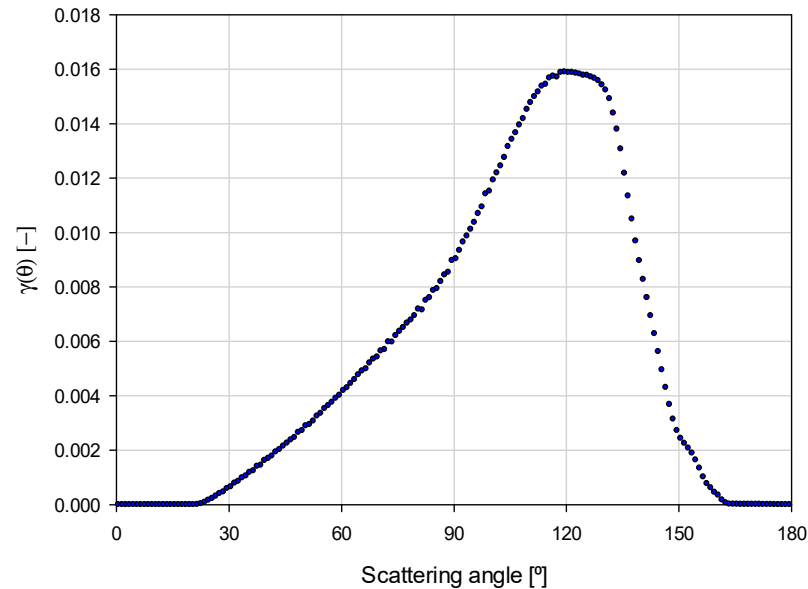


**Figure 4.** The angular weighting function  $\gamma(\theta)$  of the Seapoint turbidimeter.

Moreover, the obtained weighting function shows that the Seapoint turbidimeter has the highest sensitivity for scattering angles in a range of  $114^\circ$ – $128^\circ$ , which contains 25% of the signal. Half of the sensitivity falls in an angular range of  $102^\circ$ – $134^\circ$ . Three-quarters (75%) are located in a range of  $84^\circ$ – $140^\circ$ , and 90% in a wide range of scattering angles of  $62^\circ$  to  $146^\circ$ . Therefore, we can see a large asymmetry in the weighting function, which slopes more steeply for angles higher than  $128^\circ$ . This is 2.75 times less than the Seapoint turbidity meter's weighting function.

### 3.2. Scattering Coefficients and Volume Scattering Functions of Inorganic Suspensions

The computed scattering coefficients  $b_p$  for every size fraction of our model silica suspension are listed in the fourth column of Table 2 and shown in Figure 5a. The choice of geometric progression of the fraction boundaries caused every subsequent fraction to have an increasingly wider range of diameters and a decreasing concentration of particles, i.e., the number of particles in  $1 \text{ m}^3$  of suspension volume (see Table 2). These concentrations vary from  $1.13 \times 10^{11} \text{ m}^{-3}$  for the first fraction to  $1.9 \times 10^3 \text{ m}^{-3}$  for the last fraction, in which large particles have a diameter range of 0.146 to 0.19 mm. The total concentration of particles in all 22 fractions is  $1.98 \times 10^{11} \text{ m}^{-3}$ , while the concentration sum of the first two fractions, which define the submicron particles in our distribution, is  $1.62 \times 10^{11} \text{ m}^{-3}$ . Thus, the submicron particles account for more than 82% of the total number of particles. However, it is the micrometer-sized particles (represented by size fractions 3–11) that give the highest contribution to the scattering coefficient. The highest value of  $b_p = 1.74 \times 10^{-2} \text{ m}^{-1}$  is observed for fraction numbers 6 and 7, which have been assigned a range of diameters of 2.5 to  $3.71 \text{ }\mu\text{m}$ . This is the range of diameters that are 2.5 to over 4.2 times larger than the wavelength of the light that is scattered by these particles. In comparison, the  $b_p$  for the first particle fraction (the tiniest particles) is about 2.5 times lower and amounts to  $7.16 \times 10^{-3} \text{ m}^{-1}$ , while for the last fraction (the largest particles), the  $b_p$  coefficient is  $7.24 \times 10^{-5} \text{ m}^{-1}$  and is over 240 times lower than the highest one. Submicron particles from size fractions 1–2 account for 13% of the total scattering coefficient of the model suspension, while micrometer-sized particles (fraction numbers 3–11) account for 82% of large particles (fraction numbers 12–22) for 5% of the total  $b_p$ .

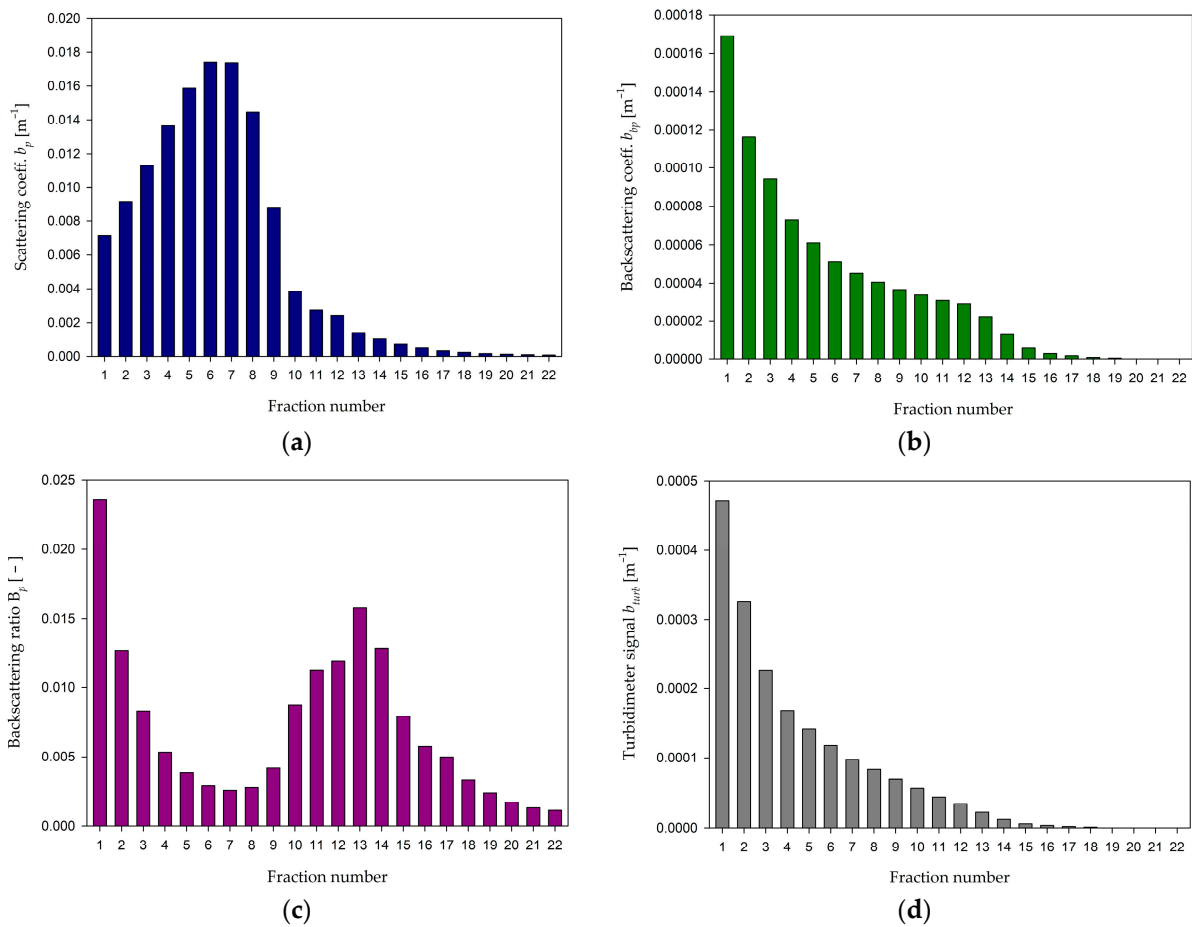


**Figure 5.** The simulated results of (a) the scattering coefficient  $b_p$ , (b) the backscattering coefficient  $b_{bp}$  and (c) the ratio  $B_p = b_{bp}/b_p$  for 22 size fractions of the model inorganic suspension. Graph (d) shows the values of  $b_{turb}$  calculated using the turbidimeter's weighting function for the same size fractions.

The backscattering coefficient  $b_{bp}$ , defined by Equation (2), is shown for all 22 fractions in Figure 5b. It shows a monotonic decrease in value for increasing suspension particle size. The highest value of  $b_{bp}$  is  $1.69 \times 10^{-4} \text{ m}^{-1}$  and occurs for fraction number 1, while the lowest value is  $8.12 \times 10^{-8} \text{ m}^{-1}$  which is found for fraction number 22. The highest value is, thus, more than 2 thousand times larger than the lowest one.

The relative backscattering coefficient  $B_p$ , which is defined by Equation (3) is depicted in Figure 5c. Moving from the smallest particles towards the larger ones, the highest value is observed for fraction number 1, and it is 0.0236. Next, for fraction number 7, a local minimum is observed for which the  $B_p$  value is 0.0026. For subsequent fractions, the values increase up to fraction number 13, where the  $B_p$  is 0.0158. Further, it monotonically decreases and reaches the minimum value of 0.0011 for fraction number 22. The highest  $B_p$  value is, therefore, only 21 times greater than the lowest one.

For a better comparison, the calculated  $b_{turb}$  values are presented in Figure 5d and further described in the Discussion section.

Angular plots of the volume scattering functions are shown in Figure 6 for selected size fractions. The angular variability of the VSFs shows the typical dependence of these functions on particle sizes [38]. Large particles scatter light more asymmetrically than small particles, showing the domination of scattering into small forward angles. This will be shown in the examples of extreme fractions, i.e., fraction number 1 (particle diameters of 0.59–0.77  $\mu\text{m}$ ) and fraction number 22 (diameters of 146–190  $\mu\text{m}$ ). The VSF value for fraction number 22 reaches  $1.62 \text{ m}^{-1}\text{sr}^{-1}$  at the scattering angle  $\theta = 0.1^\circ$ . At the same time, the lowest value of this function is  $9.5 \times 10^{-9} \text{ m}^{-1}\text{sr}^{-1}$  and it occurs for  $\theta = 158^\circ$ . The

lowest value is, therefore, 171 million times smaller than the value for  $\theta = 0.1^\circ$ , which means that forward scattering is highly dominating. It is completely different for fraction number 1. Here, the VSF value at the angle  $\theta = 0.1^\circ$  is  $6.61 \times 10^{-3} \text{ m}^{-1} \text{ sr}^{-1}$ , while the lowest VSF value is  $1.41 \times 10^{-5} \text{ m}^{-1} \text{ sr}^{-1}$  and it occurs for  $\theta = 116^\circ$ . The lowest value is, therefore, only 470 times smaller than the value for  $\theta = 0.1^\circ$ . This means that tiny particles contribute to backscattering more than others.

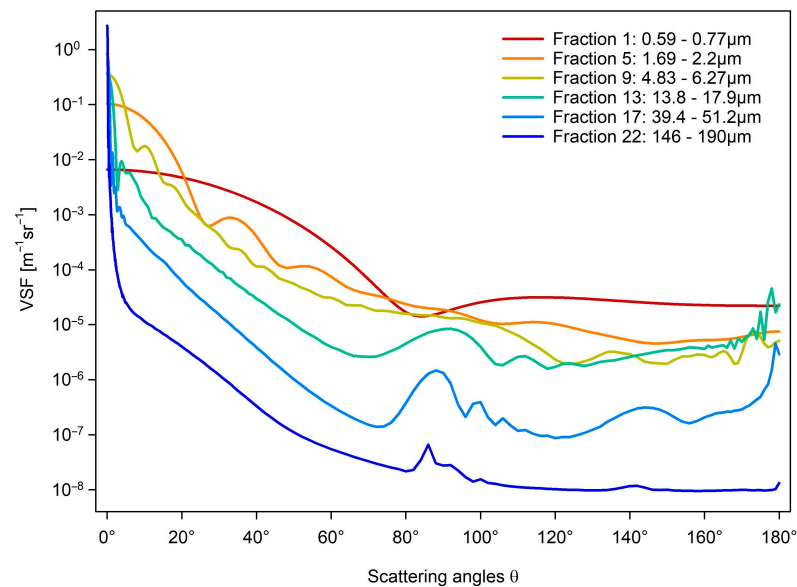


**Figure 6.** The volume scattering functions of the model suspension of silica spherical particles for selected size fractions.

#### 4. Discussion

Knowledge of the instrument's weighting function allows us to link scattering-based measurements of suspended particles to their inherent optical properties, which is necessary in environmental science, particularly in oceanography [39]. Application of weighting functions improves the accuracy of models and algorithms that relate in situ measurements to data obtained through satellite remote sensing [40,41]. This study presents the application of the Seapoint turbidimeter's weighting function in the correlation between turbidity signal and the scattering and backscattering coefficients at 880 nm for different sizes of suspended particles.

Since we had information about the VSFs for narrow-size fractions of the size distribution of the model inorganic suspension, the dependence of  $b_{turb}$  on the scattering properties was analyzed. Using Equation (3), the portion  $b_{turb}$  of the scattering coefficient  $b_p$ , measured by the turbidimeter, was calculated independently for each size fraction (see Figure 5d). The lowest value of  $b_{turb}$  is  $1.53 \times 10^{-7}$  and it was calculated based on the corresponding VSF function and  $\gamma$  function for fraction number 22. This is the fraction of the biggest particles, the diameters of which range from 146 to 190  $\mu\text{m}$ . The highest value of  $b_{turb}$  is 4580 times greater and it is  $4.72 \times 10^{-4}$ . It was obtained for fraction number 1. It is a fraction for which particle diameters are in a range of 0.59–0.77  $\mu\text{m}$ .

Figure 7a presents the variability of the  $b_{turb}$ -to- $b_p$  ratio for each of the 22 suspension fractions. The highest value of this ratio is observed for fraction number 1 and it is 0.066. The lowest value of the  $b_{turb}$ -to- $b_p$  ratio of 0.0021 is observed for the largest fraction. This value is 31 times smaller than the highest one. The plot of  $b_p$  to  $b_{turb}$  (Figure 7b) shows no straightforward linear correlation. The determination coefficient  $r^2$  here is 0.497.

The lack of correlation between  $b_{turb}$  and  $b_p$  did not satisfy the purpose of our study and led us to seek another stronger correlation. Since the angular shape of the weighting function points that 75% of the turbidity signal comes from angles higher than  $90^\circ$ , we analyzed the correlation of  $b_{turb}$  with the backscattering coefficient  $b_{bp}$  (defined by

Equation (2)). The results are plotted in Figure 8. Figure 8a shows the change in the  $b_{turb}$ -to- $b_{bp}$  ratio of all 22 fractions of the analyzed suspensions. The highest value of this ratio is 2.80 and it is observed for fraction number 2. It is a fraction for which particle diameters are in a range of 0.77–1  $\mu\text{m}$ . The lowest value of  $b_{turb}$ -to- $b_{bp}$  ratio is 0.93 and is observed for fraction number 14, for which diameters are in a range of 17.9 to 23.3  $\mu\text{m}$ . The highest value is only three times higher than the lowest one. The correlation of  $b_{bp}$ -to- $b_{turb}$  (see Figure 8b) shows a good linear relationship characterized by the determination coefficient  $r^2$  of 0.979.

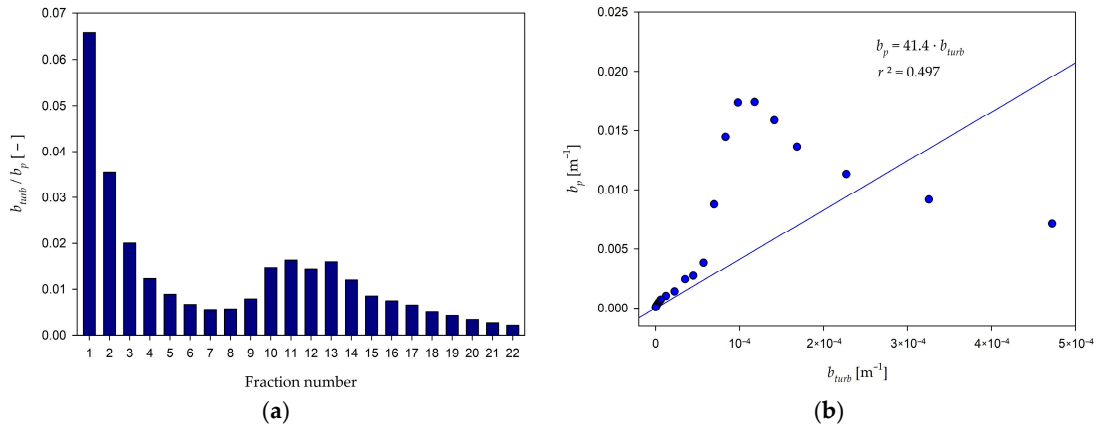


**Figure 7.** The ratio of the calculated  $b_{turb}$  of the turbidimeter to the scattering coefficient  $b_p$  for each of the 22 size fractions of the model particle suspension (a) and linear correlation of  $b_p$  to  $b_{turb}$  (b).

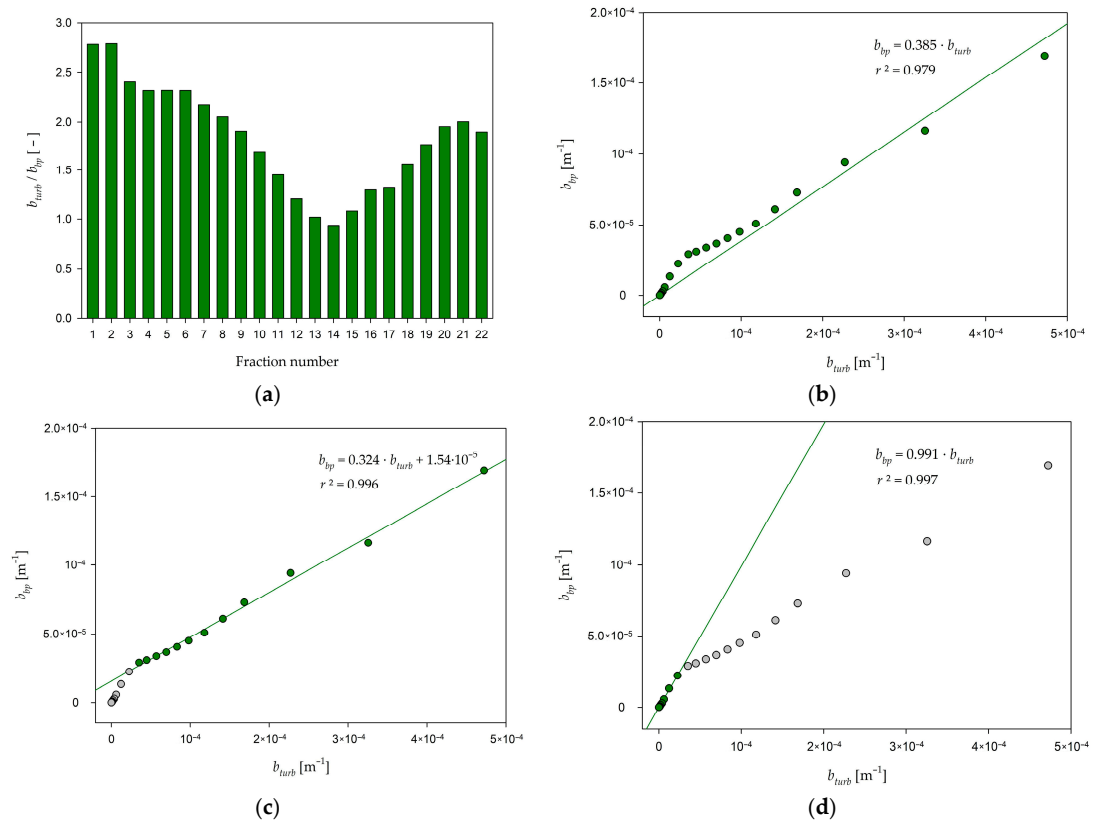


**Figure 8.** The ratio of the calculated  $b_{turb}$  of the turbidimeter to the backscattering coefficient  $b_{bp}$  for each of the 22 size fractions of the model particle suspension (a) and linear correlation of  $b_{bp}$ -to- $b_{turb}$  (b). The correlation between  $b_{bp}$  and  $b_{turb}$  for fraction numbers 1–12 (c) as well as for fraction numbers 13–22 (d).

The correlation of  $b_{bp}$ -to- $b_{turb}$  turned to be bi-modal in nature, therefore we also performed linearity analysis for two ranges of size fractions. Figure 8c shows fractions numbers 1–12, i.e.,  $b_{bp}$ -to- $b_{turb}$  correlation analysis for particles with diameters of less than 13.8  $\mu\text{m}$ . Correspondingly, Figure 8d presents the correlation for particles larger than 13.8  $\mu\text{m}$ . The  $r^2$  determination coefficients are very high in both cases, 0.996 and 0.997, respectively. For all size fractions, the backscattering coefficient may be obtained as:

$$b_{bp} = 0.385 \cdot b_{turb}. \quad (8)$$

For the fractions smaller than 13.8  $\mu\text{m}$ , more accurate relation will be

$$b_{bp} = 0.324 \cdot b_{turb} + 1.54 \times 10^{-5}, \quad (9)$$

while for the largest size fractions it will be:

$$b_{bp} = 0.991 \cdot b_{turb}. \quad (10)$$

Finally, we wanted to see how the  $b_{turb}$  signal correlates with the relative backscattering coefficient  $B_p$  (described by Equation (3)). Figure 9a includes an analysis of  $b_{turb}$ -to- $B_p$  variability for all 22 size fractions. The highest values of this ratio were obtained for fraction number 6, i.e., for particles with diameters between 2.2 and 2.86  $\mu\text{m}$ . Any smaller and larger particles gave lower values of the  $b_{turb}$ -to- $B_p$  ratio. As with the correlation with  $b_p$ , Figure 9b shows a weak linear correlation between  $B_p$  and  $b_{turb}$ . The determination coefficient  $r^2$  takes the value of 0.566, and the relationship could be approximated by straight lines if as many as three particle size ranges were considered here.

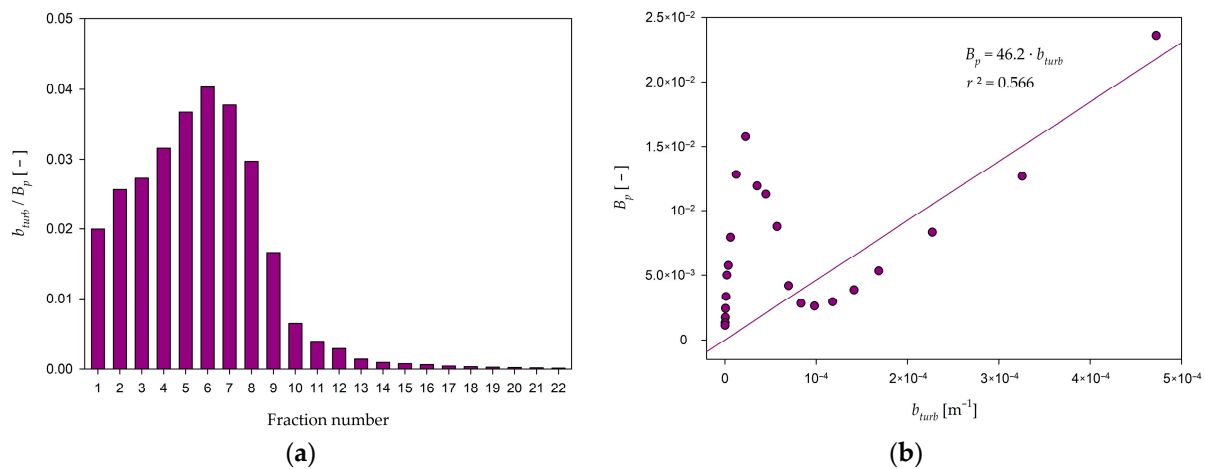


**Figure 9.** The ratio of the calculated  $b_{turb}$  of the turbidimeter to the backscattering ratio  $B_p$  for each of the 22 size fractions of the model particle suspension (a) and linear correlation of  $B_p$  to  $b_{turb}$  (b).

The weighting functions of light scattering meters similar to the one given in Figure 3 have already been studied. As early as 1990, Oishi [42] proposed, based on calculations using the Mie solution, that the backscattering coefficient be determined by measuring the light scattering for an angle of 120°. This angle corresponds to the maximum of our  $\gamma(\theta)$  function shown in Figure 3. A similar proposal was given by Ref. [43], who came up with the idea of placing a 700 nm illuminator and a detector in parallel to estimate the backscattering coefficient in natural waters. Their weighting function had a FWHM of only 20° and a maximum sensitivity at about 140°. This FWHM is 2.75 times lower than the Seapoint turbidity meter's weighting function. The subsequent analysis [44] has led to the use of single-direction scattering correlation to determine  $b_{bp}$  in commercial instruments. These included HydroScat (former HOBI Labs Inc., Bellevue, WA, USA) and EcoBB (Sea-Bird Scientific, Bellevue, WA, USA). These meters gave information on the vertical profile

of  $b_{bp}$  variability in in situ measurements when lowered to the bottom of a water body. Sullivan and Twardowski [45] proved that the variability of the VSF shape is the lowest for scattering angles between  $110^\circ$  and  $120^\circ$  and this angular range is, therefore, the best for  $b_{bp}$  estimation. For VSF measurements conducted in the Baltic Sea and oil-in-water emulsion droplets, a comparison of variability in this angle range was shown by Freda [46], who concluded that the VSF-to- $b_{bp}$  correlation is free from angular variability for an angle of  $117^\circ$  as opposed to  $140^\circ$ . Also, observations have proved that the angular VSF shapes of ocean particles, normalized by  $b_{bp}$ , show low variability at angles close to  $120^\circ$  [47].

In our analysis we chose to test the correlation between turbidity signal and the scattering coefficients on inorganic particle suspension expecting that mineral particles will scatter near-infrared light (of 880 nm) in a similar way to the visible light [34,35]. However, in natural seawater, the infrared light is strongly absorbed in water. This is why there is a need to seek for further correlations between turbidity signal and backscattering coefficient in visible light range. We expect that there will be a satisfying correlation between turbidity signal and backscattering coefficients for selected visible wavebands. There are many recent studies on correlation of the remote sensing reflectance (derived for visible wavebands) with seawater turbidity on both global and regional scales [48], and most of the proposed algorithms base on a good relationship between water turbidity and reflectance signal. Remote sensing reflectance is one of the most important apparent optical properties, known to be related to the backscattering coefficient by a simple formula  $R_{rs} \sim b_b / (a + b_b)$  [49]. Garaba et al. [30] attempted to correlate turbidity measured at 700 nm with the mean remote sensing reflectance in the spectral range 630–660 nm achieving the linear fit of  $r^2 = 0.72$ . Dogliotti et al. [50] successfully correlated turbidity measured in the North Sea at 860 nm with the corresponding reflectance signal in the near-infrared region.

Application of turbidimeter weighting function in this study additionally showed that the correlation between the inherent optical properties and turbidity signal depends on particle size structure. The analyses presented in this paper naturally hypothesize that the results of turbidity measurements conducted with the Seapoint turbidimeter will be correlated with the backscattering coefficients in the visible light range, which is of most interest to opticians working in natural waters.

## 5. Conclusions

Turbidity measurements are commonly conducted in natural waters, providing information about the transparency of these waters. Such measurements are performed with a wide variety of instruments using different geometries of the measuring system. Thus, they give a turbidity result described in different scales, which cannot be converted into the inherent optical properties. This paper takes up the idea of correlating the Seapoint turbidimeter signal with the backscattering coefficient of the sample in an exemplary model of inorganic particle suspension.

In the first step, the angular weighting function of Seapoint turbidimeter was measured using a thin steel rod placed on a mobile stand in front of turbidimeter's optical windows. Next, we created a model of silica suspension described by a typical power-law size distribution divided into 22 narrow-size fractions, from submicron to millimeter-sized particles. Then, we applied the turbidimeter weighting function to calculate the part of the scattering signal  $b_{turb}$  measured by the device. In the next step, the volume scattering functions were calculated for each size fraction and, thus, the IOPs of interest were obtained, i.e.,  $b_b$ ,  $b_{bp}$ , and  $B_p$ . The comparison with the calculated turbidity meter signal yielded the following conclusions:

- The weighting function of the Seapoint turbidimeter has the maximum sensitivity at an angle of  $120^\circ$ , which is consistent with many works [43–46] on single-angle scattering measurements for estimating the backscattering coefficient.
- This function has a high FWHM of  $55^\circ$  and 90% of the function falls in a wide range of scattering angles from  $62^\circ$  to  $146^\circ$ .

- Based on the modeling results, the turbidimeter signal has a good linear correlation with  $b_{bp}$ , but the best fit is obtained when we approximated  $b_{bp}$  separately for particles below 13.8  $\mu\text{m}$  and particles larger than 13.8  $\mu\text{m}$ .

Noteworthy is the fact that the light source for the Seapoint turbidimeter is a LED diode with a wavelength of 880 nm that is strongly absorbed in water. The next step will be to correlate  $b_{bp}$  (880) with other wavelengths in the visible range in a series of experiments performed under controlled conditions on different types of mineral and organic suspensions.

**Author Contributions:** Conceptualization, K.H., M.K. and W.F.; methodology, W.F.; software, W.F.; validation, K.H., H.T. and M.K.; formal analysis, B.P.; investigation, B.L.; resources, M.K.; data curation, W.F. and B.P.; writing—original draft preparation—K.H.; writing—review and editing—W.F.; visualization, M.K.; supervision, W.F.; project administration, W.F.; funding acquisition, H.T. All authors have read and agreed to the published version of the manuscript.

**Funding:** This research was funded by the Gdynia Maritime University team project No. WM/2023/PZ/06.

**Data Availability Statement:** The data presented in this study are available on request from the corresponding author.

**Acknowledgments:** To Dariusz Ficek and Magdalena Pawlik from the Pomeranian University of Słupsk (Poland) for their consultation and time spent on additional measurements and to Krzysztof Kwella from the Maritime Institute in Gdańsk (Poland) for setting up the measuring stand and helping with turbidity measurements.

**Conflicts of Interest:** The authors declare no conflicts of interest.

## References

1. Directive 2000/60/EC of the European Parliament and of the Council of 23 October 2000 Establishing a Framework for Community Action in the Field of Water Policy. Available online: <https://eur-lex.europa.eu/legal-content/EN/TXT/?uri=CELEX:02000L006-0-20141120#E0039> (accessed on 18 December 2023).
2. Aas, E.; Høkedal, J.; Sørensen, K. Experiments with the Secchi disk. *Ocean Sci. Discuss.* **2013**, *10*, 1833–1893.
3. Tyler, J.E. The Secchi disc. *Limnol. Oceanogr.* **1968**, *13*, 1–6. [[CrossRef](#)]
4. Preisendorfer, R.W. American Society of Limnology and Oceanography Executive Secretary. *Limnol. Oceanogr.* **1989**, *34*, 1366.
5. Renk, H.; Nakonieczny, J.; Ochocki, S.; Lorenz, Z.; Majchrowski, R.; Ficek, D. Secchi depth-chlorophyll relationship in the Baltic. *Acta Ichthyol. Piscat.* **1991**, *21*, 203–211. [[CrossRef](#)]
6. Bright, C.E.; Mager, S.M.; Horton, S.L. Predicting suspended sediment concentration from nephelometric turbidity in organic-rich waters. *River Res. Applic.* **2018**, *34*, 640–648. [[CrossRef](#)]
7. Sadar, M. Making Sense of Turbidity Measurements—Advantages in Establishing Traceability between Measurements and Technology. In Proceedings of the 2004 National Monitoring Conference, Chattanooga, TN, USA, 17–20 May 2004.
8. Lednicka, B.; Kubacka, M.; Freda, W.; Haule, K.; Dembska, G.; Galer-Tatarowicz, K.; Pazikowska-Sapota, G. Water Turbidity and Suspended Particulate Matter Concentration at Dredged Material Dumping Sites in the Southern Baltic. *Sensors* **2022**, *22*, 8049. [[CrossRef](#)]
9. Dera, J. *Marine Physics*; PWN: Warsaw, Poland, 2003; pp. 1–514.
10. Pawlik, M.M.; Ficek, D. Validation of measurements of pine pollen grain concentrations in Baltic Sea waters. *Oceanologia* **2022**, *64*, 233–243. [[CrossRef](#)]
11. Pawlik, M.M.; Ficek, D. Spatial Distribution of Pine Pollen Grains Concentrations as a Source of Biologically Active Substances in Surface Waters of the Southern Baltic Sea. *Water* **2023**, *15*, 978. [[CrossRef](#)]
12. Constantin, S.; Doxaran, D.; Constantinescu, S. Estimation of water turbidity and analysis of its spatio-temporal variability in the Danube River plume (Black Sea) using MODIS satellite data. *Cont. Shelf Res.* **2016**, *112*, 14–30. [[CrossRef](#)]
13. Bin Omar, A.F.; Bin MatJafri, M.Z. Turbidimeter Design and Analysis: A Review on Optical Fiber Sensors for the Measurement of Water Turbidity. *Sensors* **2009**, *9*, 8311–8335. [[CrossRef](#)] [[PubMed](#)]
14. Haule, K.; Toczek, H.; Borzycka, K.; Darecki, M. Influence of Dispersed Oil on the Remote Sensing Reflectance—Field Experiment in the Baltic Sea. *Sensors* **2021**, *21*, 5733. [[CrossRef](#)] [[PubMed](#)]
15. Baszanowska, E.; Otremba, Z.; Piskozub, J. Modelling Remote Sensing Reflectance to Detect Dispersed Oil at Sea. *Sensors* **2020**, *20*, 863. [[CrossRef](#)]
16. Sadar, M. *Turbidimeter Instrument Comparison: Low-Level Sample Measurement*; Technical Information Series No. 7063; Hach Company: Loveland, CO, USA, 1999.
17. Anderson, C.W. Chapter A6. Section 6.7. Turbidity. In *Techniques of Water-Resources Investigations 09-A6.7*; Version 2.1; U.S. Geological Survey: Reston, VA, USA, 2005; pp. 1–55.

18. Haule, K.; Freda, W. Remote Sensing of Dispersed Oil Pollution in the Ocean—The Role of Chlorophyll Concentration. *Sensors* **2021**, *21*, 3387. [[CrossRef](#)] [[PubMed](#)]
19. Rymaszewicz, A.; O’Sullivan, J.J.; Bruen, M.; Turner, J.N.; Lawler, D.M.; Conroy, E.; Kelly-Quinn, M. Measurement differences between turbidity instruments, and their implications for suspended sediment concentration and load calculations: A sensor inter-comparison study. *J. Environ. Manag.* **2017**, *199*, 99–108. [[CrossRef](#)] [[PubMed](#)]
20. Gray, J.R.; Gartner, J.W. Technological advances in suspended-sediment surrogate monitoring. *Water Resour. Res.* **2009**, *45*, 1–20. [[CrossRef](#)]
21. Gray, J.R.; Glysson, G.D. (Eds.) *Proceedings of the Federal Interagency Workshop on Turbidity and Other Sediment Surrogates, Reno, Nevada, USA, 30 April 30–2 May 2002*; Circular 1250; U.S. Geological Survey: Reston, VA, USA, 2003; pp. 1–56.
22. Merten, G.H.; Capel, P.D.; Minella, J.P.G. Effects of suspended sediment concentration and grain size on three optical turbidity sensors. *J. Soils Sediments* **2014**, *14*, 1235–1241. [[CrossRef](#)]
23. Trevathan, J.; Read, W.; Sattar, A. Implementation and Calibration of an IoT Light Attenuation Turbidity Sensor. *Internet Things* **2022**, *19*, 100576. [[CrossRef](#)]
24. EPA/600/R-93/100; Methods for the Determination of Inorganic Substances in Environmental Samples. U.S. Environmental Protection Agency: Cincinnati, OH, USA, 1993; pp. 1–178.
25. ISO 7027:1999(en); Water Quality—Determination of Turbidity. International Organization for Standardization: Geneva, Switzerland, 1999; pp. 1–10.
26. Gohin, F.; Bryère, P.; Lefebvre, A.; Sauriau, P.-G.; Savoye, N.; Vantrepotte, V.; Bozec, Y.; Cariou, T.; Conan, P.; Coudray, S.; et al. Satellite and In Situ Monitoring of Chl-a, Turbidity, and Total Suspended Matter in Coastal Waters: Experience of the Year 2017 along the French Coasts. *J. Mar. Sci. Eng.* **2020**, *8*, 665. [[CrossRef](#)]
27. Ouillon, S.; Douillet, P.; Andréfouët, S. Coupling satellite data with in situ measurements and numerical modeling to study fine suspended-sediment transport: A study for the lagoon of New Caledonia. *Coral Reefs* **2004**, *23*, 109–122.
28. Jafar-Sidik, M.; Gohin, F.; Bowers, D.; Howarth, J.; Hull, T. The relationship between suspended particulate matter and turbidity at a mooring station in a coastal environment: Consequences for satellite-derived products. *Oceanologia* **2017**, *59*, 365–378. [[CrossRef](#)]
29. Münzberg, M.; Hass, R.; Dinh Duc Khanh, N.; Reich, O. Limitations of turbidity process probes and formazine as their calibration standard. *Anal. Bioanal. Chem.* **2017**, *409*, 719–728. [[CrossRef](#)] [[PubMed](#)]
30. Garaba, S.P.; Badewien, T.H.; Braun, A.; Schulz, A.-C.; Zielinski, O. Using ocean colour remote sensing products to estimate turbidity at the Wadden Sea time series station Spiekeroog. *J. Eur. Opt. Soc.—Rapid Publ.* **2014**, *9*, 14020. [[CrossRef](#)]
31. Wang, Y.W.; Peng, Y.; Du, Z.; Lin, H.; Yu, Q. Calibrations of suspended sediment concentrations in high-turbidity waters using different in situ optical instruments. *Water* **2020**, *12*, 3296. [[CrossRef](#)]
32. Mobley, C.D. *Light and Water: Radiative Transfer in Natural Waters*; Academic Press: Cambridge, MA, USA, 1994; pp. 1–592.
33. Mie, G. Beiträge zur Optik trüber Medien, speziell kolloidaler Metallösungen. *Ann. Phys.* **1908**, *330*, 377–445. [[CrossRef](#)]
34. Bohren, C.F.; Huffman, D.R. *Absorption and Scattering of Light by Small Particles*; John Wiley & Sons: Hoboken, NJ, USA, 1983; pp. 1–533.
35. Jonasz, M.; Fournier, G.R. *Light Scattering by Particles in Water*; Academic Press: Cambridge, MA, USA, 2007; pp. 1–714.
36. Available online: <https://www.britannica.com/science/clay-mineral> (accessed on 6 February 2024).
37. Rodríguez-de Marcos, L.V.; Larruquert, J.I.; Méndez, J.A.; Aznárez, J.A. Self-consistent optical constants of SiO<sub>2</sub> and Ta<sub>2</sub>O<sub>5</sub> films. *Opt. Mater. Express* **2016**, *6*, 3622–3637. [[CrossRef](#)]
38. Haule, K.; Freda, W. The effect of dispersed Petrobaltic oil droplet size on photosynthetically active radiation in marine environment. *Environ. Sci. Pollut. Res.* **2016**, *23*, 6506–6516. [[CrossRef](#)] [[PubMed](#)]
39. Santalices, D.; de Castro, A.J.; Briz, S. New Method to Calculate the Angular Weighting Function for a Scattering Instrument: Application to a Dust Sensor on Mars. *Sensors* **2022**, *22*, 9216. [[CrossRef](#)]
40. Heintzenberg, J.; Wiedensohler, A.; Tuch, T.; Covert, D.; Sheridan, P.; Ogren, J.; Gras, J.; Nessler, R.; Kleefeld, C.; Kalivitis, N.; et al. Intercomparisons and aerosol calibrations of 12 commercial integrating nephelometers of three manufacturers. *J. Atmos. Ocean. Technol.* **2006**, *23*, 902–914. [[CrossRef](#)]
41. McKee, D.; Piskozub, J.; Röttgers, R.; Reynolds, R.A. Evaluation and Improvement of an Iterative Scattering Correction Scheme for in situ Absorption and Attenuation Measurements. *J. Atmos. Ocean. Technol.* **2013**, *30*, 1527–1541. [[CrossRef](#)]
42. Oishi, T. Significant relationship between the backward scattering coefficient of sea water and the scatterance at 120°. *Appl. Opt.* **1990**, *29*, 4658–4665. [[CrossRef](#)]
43. Maffione, R.A.; Dana, D.R. Instruments and methods for measuring the backward-scattering coefficient of ocean waters. *Appl. Opt.* **1997**, *36*, 6057–6067. [[CrossRef](#)]
44. Boss, E.; Pegau, W.S. Relationship of light scattering at an angle in the backward direction to the backscattering coefficient. *Appl. Opt.* **2001**, *40*, 5503–5507. [[CrossRef](#)] [[PubMed](#)]
45. Sullivan, J.M.; Twardowski, M.S. Angular shape of the oceanic particulate volume scattering function in the backward direction. *Appl. Opt.* **2009**, *48*, 6811–6819. [[CrossRef](#)] [[PubMed](#)]
46. Freda, W. Spectral dependence of the correlation between the backscattering coefficient and the volume scattering function measured in the southern Baltic Sea. *Oceanologia* **2012**, *54*, 355–367. [[CrossRef](#)]
47. Zhang, X.; Boss, E.; Gray, D.J. Significance of scattering by oceanic particles at angles around 120 degree. *Opt. Express* **2014**, *22*, 31329–31336. [[CrossRef](#)] [[PubMed](#)]

48. Zheng, L.; Qiu, Z.; Zhou, Y.; Sun, D.; Wang, S.; Wu, W.; Perrie, W. Comparisons of algorithms to estimate water turbidity in the coastal areas of China. *Int. J. Remote Sens.* **2016**, *37*, 6165–6186. [[CrossRef](#)]
49. Gordon, H.R.; Brown, O.B.; Jacobs, M.M. Computed relationship between the inherent and apparent optical properties of a flat homogeneous ocean. *Appl. Optics* **1975**, *14*, 417–427. [[CrossRef](#)]
50. Dogliotti, A.I.; Ruddick, K.G.; Nechad, B.; Doxaran, D.; Knaeps, E. A single algorithm to retrieve turbidity from remotely-sensed data in all coastal and estuarine waters. *Remote Sens. Environ.* **2015**, *156*, 157–168. [[CrossRef](#)]

**Disclaimer/Publisher’s Note:** The statements, opinions and data contained in all publications are solely those of the individual author(s) and contributor(s) and not of MDPI and/or the editor(s). MDPI and/or the editor(s) disclaim responsibility for any injury to people or property resulting from any ideas, methods, instructions or products referred to in the content.